High Resolution Biomolecular Condensate Phase Diagrams with a Combinatorial Microdroplet Platform

William E. Arter,[1],[†] Runzhang Qi,[1],[†] Nadia A. Erkamp,[1],[†] Georg Krainer,[1],[†] Kieran Didi,[1] Timothy J. Welsh,[1] Julia Acker,[2] Jonathan Nixon-Abell,[3] Seema Qamar,[3] Jordina Guillén-Boixet,[4] Titus M. Franzmann,[4] David Kuster,[5] Anthony A. Hyman,[5] Alexander Borodavka,[2] Peter St George-Hyslop,[3,6,7] Simon Alberti[4] and Tuomas P.J. Knowles[1,8,*]

[1] *Yusuf Hamied Department of Chemistry, Centre for Misfolding Diseases, University of Cambridge, Lensfield Road, Cambridge, CB2 1EW, UK*

[2] *Department of Biochemistry, University of Cambridge, Cambridge, CB2 1QW, UK*

[3] *Cambridge Institute for Medical Research, Department of Clinical Neurosciences, University of Cambridge, Cambridge CB2 0XY, UK*

[4] *Biotechnology Center (BIOTEC), Center for Molecular and Cellular Bioengineering (CMCB), Technische Universität Dresden, Tatzberg 47/49, 01307 Dresden, Germany*

[5] *Max Planck Institute for Molecular Cell Biology and Genetics, Pfotenhauerstrasse 108, 01307 Dresden, Germany*

[6] *Department of Medicine (Division of Neurology), University of Toronto and University Health Network, Toronto, Ontario M5S 3H2, Canada*

[7] *Department of Neurology, Columbia University, 630 West 168th St , New York, NY 10032, USA.*

[8] *Cavendish Laboratory, Department of Physics, University of Cambridge, J J Thomson Ave, Cambridge, CB3 0HE, UK*

[†] These authors contributed equally.

* To whom correspondence should be addressed:
E-mail: tpjk2@cam.ac.uk

Abstract

The assembly of intracellular proteins into biomolecular condensates is a fundamental process underlying the organisation of intracellular space and the regulation of many cellular processes. Mapping and characterising phase behaviour of biomolecules is essential to understand the mechanisms of condensate assembly, and to develop therapeutic strategies targeting biomolecular condensate systems. A central concept for characterising phase-separating systems is the phase diagram. Phase diagrams are typically built from numerous individual measurements sampling different parts of the parameter space. However, even when performed in microwell plate format, this process is slow, low throughput and requires significant sample consumption. To address this challenge, we present here a combinatorial droplet microfluidic platform, termed PhaseScan, for rapid and high-resolution acquisition of multidimensional biomolecular phase diagrams. Using this platform, we characterise the phase behaviour of a wide range of systems under a variety of conditions and demonstrate that this approach allows the quantitative characterisation of the effect of small molecules on biomolecular phase transitions.

Introduction

Many cellular proteins have the ability to demix into a protein-rich liquid condensate phase and a protein-depleted diluted phase.[1] This liquid–liquid phase separation (LLPS) process, has emerged as a fundamental mechanism to describe the formation of biological condensates in living cells.[2] Condensates systems such as stress granules, paraspeckles, and nuclear bodies are formed by LLPS and compartmentalise cellular space.[3] They act as microreactors for biochemical reactions,[4] and are crucial to a wide range of physiological processes such as gene expression, signalling, and metabolic regulation.[5–7] Condensate-forming proteins are also heavily implicated in protein misfolding diseases including motor neuron disease,[8–10] cancer pathogenesis[11] and infectious diseases,[12] making them attractive targets for therapeutic intervention.[13,14]

Phase separation, now established for hundreds of cellular proteins,[15] can be triggered by variations in environmental conditions such as changes in ionic strength, pH, temperature, molecular crowding, and the presence of small molecules.[16–21] It is important that cellular concentrations of condensate components are considered during in-vitro analysis, given the high sensitivity of cellular phase separation to parameters such as protein concentration.[22] Because of this sensitivity to physicochemical parameters, there is great potential to modulate protein phase separation in a targeted manner and many phase separating proteins and their complexes are receiving intense interest as fundamentally novel drug targets to ameliorate human diseases.[23,24] However, it remains challenging to quantify the physical parameters that modulate phase separation behaviour in LLPS systems with high fidelity, accuracy and throughput.[16]

A central concept that characterises phase-separating systems is the phase diagram.[24–26] Phase diagrams summarise the phase behaviour of condensates by monitoring the position of the transition between the phase-separated and the mixed regimes through determination of the position of the phase boundary in chemical space.[27] Changes in the phase boundary for an LLPS system following variation of solution conditions affords insights to the thermodynamic processes driving protein condensation and the factors that modulate them.[17] However, given the large variety of proteins undergoing LLPS and the environmental conditions which regulate their behaviour, there is a need for experimental methods that enable rapid and high-resolution characterisation of LLPS phase diagrams. Typically, these are generated by labour and time intensive methods involving the stepwise combination of reagents to create the requisite variation in solution conditions before observation of individual conditions by microscopy.

Notably, although phase diagrams are often used to probe the behaviour of LLPS systems, such experiments can only provide a coarse-grained picture of the protein phase-space when conducted manually.[28,29]

To address this challenge, we describe here a droplet microfluidic approach, PhaseScan, that enables rapid, automated generation of different LLPS solution conditions for high-resolution assessment of protein LLPS behaviour. Lab-on-a-chip microfluidic systems, in particular microdroplet-based formats, offer an effective means to improve assay throughput, parallelisation, and miniaturisation in biochemical experiments. To date these platforms have been leveraged to probe protein phase behaviour [30–33] by concentration or evaporation of dilute, homogeneous protein solutions contained in microwells or microdroplets, so that the system becomes sufficiently concentrated to pass into the phase-separated regime. Initiating phase separation by concentrating the solution means that salt and buffer are also concentrated, making it challenging to probe phase diagrams under fully physiological conditions or to map out phase diagrams without chemical or physical dimensions being interdependent.

We aim to overcome these challenges through combinatorial droplet microfluidics to rapidly generate a large number of independent micro-compartments, each of which can be considered a discrete environment in which to study protein LLPS. This approach allows a far greater number of unique conditions to be probed than alternative microfluidic approaches where assay components are passively mixed and compartmentalised by the fluidic device itself. Such formats limit the number of distinct solution conditions that can be assayed by the extent and complexity of the fluidic network that is possible and practical to operate.[33–35] PhaseScan, by contrast, alters the input solution conditions in a combinatorial manner during droplet encapsulation, allowing for rapid generation of an arbitrary number of phase separation microenvironments to map LLPS behaviour over a broad range of chemical space. We demonstrate the operation of the PhaseScan platform by acquiring phase diagrams for a variety of phase-separating proteins and their modulation by molecular crowding, salt concentration, and nucleic acid concentration. We then investigate and compare the effect of small molecules on the protein phase separation. Finally, we show the acquisition of a three-dimensional phase diagram, demonstrating the potential of our platform for parallelised, multi-dimensional analysis of chemical space in the context of protein phase separation.

Results and Discussion

Working principle of the PhaseScan platform

First, we implemented a workflow for microdroplet generation and imaging (Figure 1(a)). As a model system, we utilised an EGFP-tagged G156E mutant of the protein fused in sarcoma (FUS^{G156E}), a protein implicated in the pathology of amyotrophic lateral sclerosis (ALS) that has previously been shown to phase separate .[9,36] Phase separation was triggered by molecular crowding with polyethylene glycol (PEG), as reported previously.[9]
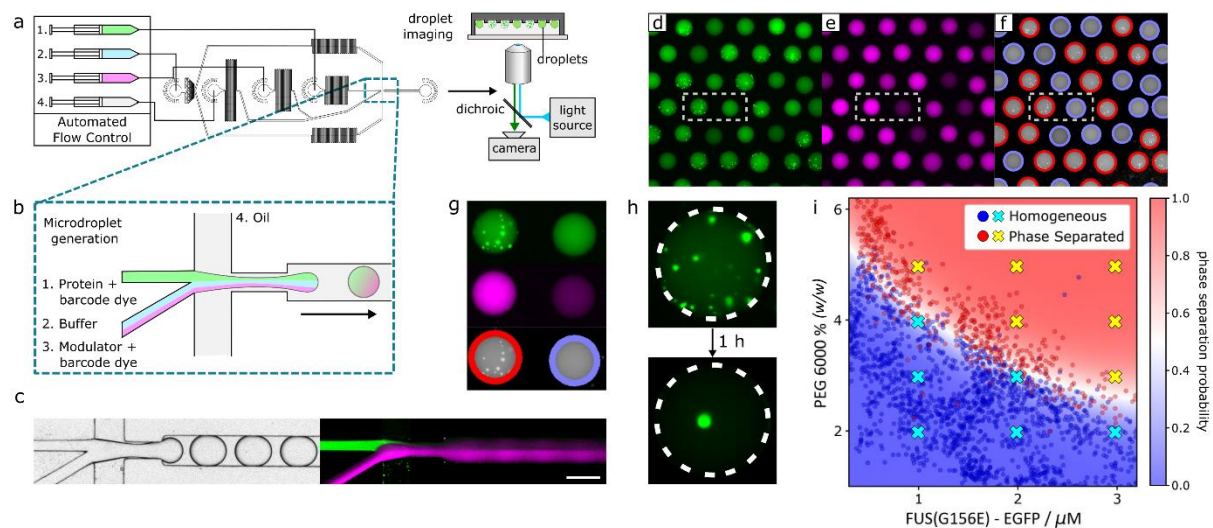

Figure 1: PhaseScan workflow.

(a) Droplets are generated using a flow-focussing microfluidic device controlled by automated syringe pumps and then imaged in wells by fluorescence microscopy. **(b)** At the droplet generating junction, aqueous solutions are combined under laminar flow before droplet formation. **(c)** Brightfield microscopy image of droplet generation (left) and combined fluorescence images of droplet generation (right) showing fluorescence of EGFP (green) and Alexa647 (magenta) barcodes for FUS^{G156E} and PEG, respectively. **(d, e)** Epifluorescence microscopy images of trapped microdroplets, with EGFP and Alexa647 fluorescence corresponding to FUS^{G156E} and PEG concentration, respectively. **(f)** Classification of droplets as phase separated (red outline) or homogeneous (blue outline) according to distribution of EGFP fluorescence. **(g)** Phase separated (left) and homogeneous (right) microdroplets imaged according to EGFP (top) and Alexa647 fluorescence (middle) and subsequent phase separation classification (bottom). Images correspond to the highlighted regions in (d-f). **(h)** Liquid condensates merge over time in microdroplets. **(i)** Phase diagram of EGFP-FUS^{G156E} vs. PEG 6000 concentration, 50 mM Tris pH 7.4, 150 mM KCl. Red and blue data points in the scatter plot correspond to individual microdroplets classified as phase separated or homogeneous, respectively. The heat map corresponds to the probability of phase separation as determined by an SVM classifier trained on the droplet scatter plot. N = 2754 droplets. Yellow and cyan crosses correspond to phase separated and homogeneous behaviour as determined by manual pipetting experiment.

Aqueous solutions containing protein, buffer, and the modulator PEG were mixed in different ratios on chip prior to encapsulation in water-in-oil microcompartments of ~700 pL

in volume dispersed in an immiscible fluorinated-oil continuous phase (Figure 1(b)). Due to laminar flow, the aqueous solutions do not mix significantly before droplet formation,[37] and droplet coalescence is prevented by supplementing the fluorinated oil phase with a biologically compatible polyglycerol-based triblock surfactant (see Methods).[38] The relative flow rates of the aqueous solutions are altered while the total flow rate is kept constant using a programme controlled by an automated syringe pump system. This enables the formation of droplets containing protein and PEG concentrations over a range of chemical space. To determine the amount of protein and PEG present in each droplet in downstream analysis, the concentration of each of these components was barcoded by a particular fluorophore (Figure 1(b, c)). For FUS^{G156E}, this information was provided by its EGFP tag, whereas the concentration of PEG was barcoded by Alexa647 dye pre-mixed into the PEG starting solution (see Methods).

Following generation, droplets were collected in a PDMS gravity-trap device, that utilises the lower density of droplets in comparison to the surrounding oil to immobilise droplets in microwells contained in the roof of a flow chamber, as described previously.[30,39] Approximately 2600 droplets were collected per experiment, with droplet generation occurring over a timescale that allowed at least two repetitions of the flow programme to ensure that the full range of conditions were scanned, before undergoing epifluorescence microscopy imaging according to the fluorescence wavelengths of each of the barcode fluorophores (Figure 1(d, e)). According to the barcode fluorescence intensity, the corresponding concentrations of protein or PEG were determined on a per-droplet basis by comparison to a calibration measurement of known fluorophore concentration (see Methods, Figure S9).

Droplets were then classified as phase-separated or homogeneous according to the presence or absence of condensates visualised via the protein EGFP tag (Figure S10). Figure 1(g, f) demonstrates the assignment for a representative image of phase-separated and homogeneous droplets containing EGFP-FUS^{G156E}, with a red or blue outline indicating classification of droplets as phase separated or homogeneous, respectively. Typically, the sum of false-positive and false-negative classification error by our algorithm is < 4% of the total number of droplets classified, although this value varies slightly depending on the signal to noise ratio of condensate fluorescence for the system in question.

We observed merging of condensates over time (Figure 1h), which together with off-chip fluorescence recovery after photobleaching (FRAP) experiments (Supporting Information, Figure S1) confirmed the liquid nature of condensates formed in the PhaseScan experiment. By combining the determined concentration and the presence or absence of phase separation

as a scatter plot on a per-droplet basis, a phase diagram was produced (Figure 1(i)). The position of the phase boundary and probability of phase separation as a function of EGFP-FUS^{G156E} and PEG concentration was then determined by a support-vector machine (SVM) algorithm trained on the scatter-plot populations of phase-separated or homogeneous droplets (Figure 1(i), see Methods). Notably, only a technique with sufficient throughput allows the use of statistical methods to comprehensively and continuously describe phase behaviour in the manner demonstrated here.

We observe that droplets can be classified robustly into phase separated or homogeneous regions according to concentrations of FUS^{G156E} and PEG that show excellent agreement with previous studies.[9] The homotypic phase separation of wild-type EGFP-FUS was also assessed and similar behaviour was observed (data not shown). To assess whether the phase-behaviour of FUS^{G156E} was notably altered by droplet encapsulation, the presence or absence of phase separation under the same conditions as those probed by PhaseScan were confirmed as the same in bulk volumes by manual pipetting experiments (Figure 1(i) and Figure S2). Importantly, although the phase-separation systems described herein are characterised by use of fluorophore-tagged proteins, this is not a pre-requisite for operation of the PhaseScan platform as the presence of condensates within droplets could instead be observed by brightfield microscopy as shown elsewhere[30,33] and in Figure S1.

To test whether the barcoding dyes affect the phase boundary, the phase behaviour of FUS^{G156E} was assessed as a function of Alexa546 and Alexa647 dye concentration (Supporting Information, Figure S3). No significant effect was observed, with phase separation propensity remaining unchanged for the barcode concentrations used here (< 6.5 µM, see Methods).

Phase separated systems behave dynamically, with condensate droplets evolving after nucleation due to growth, coalescence and Ostwald ripening.[40,41] To test whether these processes effect the accuracy of the PhaseScan measurement, phase diagrams for homotypic FUS phase separation were generated in triplicate, with droplet generation proceeding continuously but with 30 min between data acquisition for each replicate measurement. Only negligible differences were observed between the replicates (Figure S4), demonstrating that the PhaseScan protocol described here (> 5 min between drop generation and imaging) allows sufficient time between droplet generation and measurement for the assay to accurately and reproducibly assess the equilibrium phase boundary position. This is in agreement with previous findings, where the characteristic timescale for condensate formation within droplets of >100 nL was found to be < 1 min.[42]

We also investigated the potential for droplet size to affect the reported position of the phase boundary, since droplet volume has the propensity to modulate the dynamics of nucleation-driven condensate growth.[42] Phase diagrams for homotypic FUS[G156E] condensates were recorded using droplets of two different sizes with mean volumes of 0.33 and 1.1 nL, which bracketed the typical droplet volume of 0.65 nL used in PhaseScan experiments (Supporting Information, Figure S5). No difference was observed between these phase diagrams, which together with the lack of time-dependence in the PhaseScan output described above, indicates that the PhaseScan experiment reports the quilibrium position of the phase boundary and is insensitive to droplet volume.

Notably, the PhaseScan technique provides throughput several orders of magnitude higher than manual experiments in terms of the number of unique conditions investigated, with >2500 droplets assayed per experiment. Reagent consumption is minimal, with < 2 µL of stock protein solution used per assay, although we found that a minimum working volume of 10 µL was required for effective operation (see Methods). Moreover, data generation is rapid, with droplet generation and collection requiring approximately 5 min. This is in contrast to microfluidic approaches for investigation of LLPS based on droplet shrinking, which can require experimental timescales of several hours.

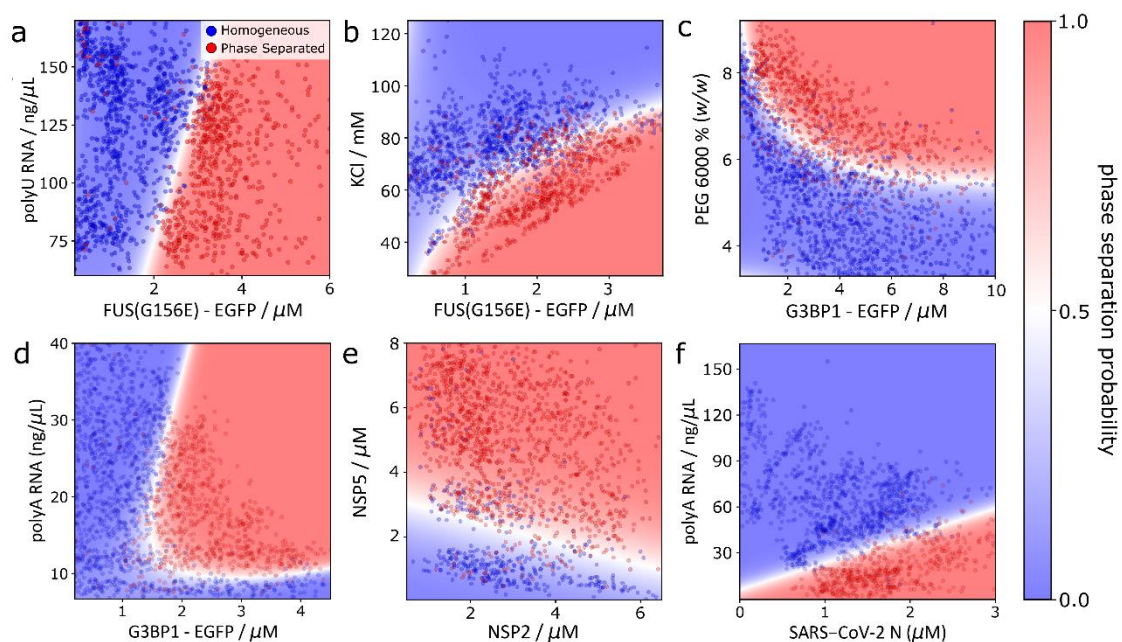## PhaseScan is generalisable to a range of phase-separating systems

Figure 2: Application of PhaseScan to a variety of condensate systems. (a) Phase diagram of EGFP-tagged FUS[G156E] vs. polyU RNA concentration. N = 2096 droplets. **(b)** Phase diagram of FUS[G156E]

8

condensation as a function of protein and salt concentration. N = 2625 droplets. **(c)** Phase diagram of EGFP-tagged G3BP1 vs. PEG 6000 concentration. N = 2549 droplets. **(d)** Phase diagram for coacervation-condensation of rotavirus proteins NSP2 and NSP5. N = 1672 droplets. **(e)** Phase diagram for polyA RNA-mediated phase separation of SARS-CoV-2 N protein. N = 1599 droplets. **(f)** Phase diagram for polyA RNA-mediated phase separation G3BP1. N = 3017 droplets

Having validated the operation of the PhaseScan system, we then sought to utilise our platform for the investigation of a range of phase-separating systems and test the generality of the method for homotypic and heterotypic condensate systems.

Since coacervation of nucleic acids is a defining characteristic of phase-separated ribonucleoprotein granules, we began by producing a phase diagram for condensation of EGFP-tagged FUS^{G156E} in the presence of polyU RNA (Figure 2(a)). As observed previously,[43] no phase separation was detected at low ratios of FUS^{G156E} relative to RNA, with phase-separation then occurring at higher FUS^{G156E} concentrations. Notably, the phase boundary appears highly linear, in agreement with studies that suggest that condensate formation and protein–RNA coacervation occurs via charge neutralisation,[43] and that condensation therefore occurs at a discrete ratio of RNA to protein.

Next, we generated a phase diagram for the phase separation of FUS^{G156E} as a function of KCl concentration (Figure 2(b)). In agreement with previous findings, FUS^{G156E} was observed to possess an increased propensity for phase separation at high protein and low salt concentrations. Analysis of the effect of ionic strength on the propensity of condensate systems to phase separate can afford mechanistic insight into the molecular-level interactions that drive LLPS, by elucidating the extent to which phase separation, for example, is influenced by electrostatic interactions.[44,45] We therefore envisage that PhaseScan could enable rapid, high-resolution mechanistic analysis of phase separation processes.

To demonstrate the applicability of the PhaseScan system to other phase separating proteins, we next characterised the crowding-driven phase separation of EGFP-tagged G3BP1, a scaffolding protein required for the formation of stress granules (Figure 2(c)).[46] As expected, phase separation of G3BP1 was present at high concentrations of PEG molecular crowder, with this effect enhanced at higher protein concentration.

We then applied the PhaseScan assay to study reentrant phase behaviour, a central concept in the LLPS field. Formation of ribonucleoprotein condensates is largely driven by favourable electrostatic interactions between protein and RNA. However, at sufficiently high ratio of RNA to protein, charge inversion leads to condensate dissociation and a reentrant phase transition to

a homogenous, single phase regime.[43,47] By varying the mixing ratio of G3BP1 and polyA RNA in a PhaseScan experiment, we observed reentrant phase behaviour of the resultant coacervate condensate (Figure 2(d)). At a G3BP1 concentration of 1.8 µM, the system transitioned into and out of a phase separated regime as the RNA concentration was varied between 7 – 40 ng/µL. This observation demonstrates the power of the PhaseScan technique, in accurately characterising reentrant phase transitions in a single experiment.

We then assayed the formation of phase separated protein–protein coacervates by investigating the condensation of rotavirus proteins NSP2 and NSP5 (Figure 2(e)). These proteins are key constituents of membraneless viral replication factories known as the viroplasm; recent studies suggest that LLPS provides a mechanism for viroplasm construction.[48,49] In agreement with these findings, and in support of a recent study demonstrating coacervation of NSP2 and NSP5 both in vivo and in vitro,[50] we observe condensation of NSP2 and NSP5 in a concentration-dependent manner, with an NSP2-dependent threshold of NSP5 relative to NSP2 required for LLPS to occur.

Finally, we probed phase separation of the nucleocapsid protein of the human coronavirus SARS-CoV-2 (SARS-CoV-2 N) (Figure 2(f)). In accordance with previous findings,[51,52] we observe phase separation in an RNA-dependent manner. The ordinarily homogeneous SARS-CoV-2 N protein phase separated in the presence of polyA RNA concentrations below 25 ng/µL, however no phase separation was visible at RNA concentration above 65 ng/µL. The exact position of the phase boundary varied according to SARS-CoV-2 N concentration, with a higher protein concentration requiring a correspondingly higher concentration of RNA for phase separation to be ablated. These results are in agreement with previous studies, which have shown through manual experiments that phase separation of SARS-CoV-2 N can be driven by the presence of RNA, but that excess nucleic acid concentrations result in condensate dissolution.[52]

In summary, these experiments demonstrate that the PhaseScan approach is applicable to a broad range of condensate systems. The assay can be used to characterise homo- and heterotypic phase separation of full-length proteins, including the observation of re-entrant phase separation behaviour in protein-RNA coacervates. PhaseScan can also characterise phase separation driven by protein-protein coacervates, as well as LLPS of short peptide sequences, which we demonstrate by examining the phase separation of the proline-arginine dipeptide (PR)$_{25}$ with polyU RNA (Figure S6).

Observation of small-molecule modulation of phase separation

Next, we applied our platform to the investigation of the effect of small molecules on phase separation. There is great interest in identifying compounds that modulate LLPS as condensate forming processes are associated with a wide range of diseases, including neurodegenerative disorders and cancer.[14,53–55] Critical to this effort is the provision of high-resolution phase diagrams for the accurate quantification of the effect of small-molecule modulators on the phase separation equilibrium. Moreover, for high-throughput screening of drug candidates, it is imperative that the phase diagram for a particular drug–protein combination is acquired rapidly. The PhaseScan platform brings together these features and enables fast, automated generation of different LLPS solution conditions for high-resolution assessment of changes in protein LLPS behaviour.

To establish the applicability of the PhaseScan system for probing the effects of small-molecule compounds, we first determined the modulation of FUS^{G156E} phase separation by the small molecule 4,4′-dianilino-1,1′-binaphthyl-5,5′-disulfonic acid (bis-ANS), a compound which has recently been shown to act as a potent modulator of various phase separating proteins, including the FUS low-complexity domain.[55] To this end, we modified the microdroplet generator to allow the addition of a fourth solution component to the PhaseScan experiment (Figure S7), which in this case contained the small-molecule modulator bis-ANS. This solution was injected into the PhaseScan experiment at a constant flowrate, in addition to EGFP-tagged FUS^{G156E}, PEG and buffer solutions at varying flow rates, to achieve an equal concentration of the small molecule in each droplet (see Methods). Bis-ANS was at a concentration of 1 mM (in 1% DMSO) and was diluted 10-fold on chip to results in a final concentration of $100\,\mu M$ (0.1% DMSO) in the droplet. As a control, we performed an experiment without bis-ANS but with buffer supplemented with 1% DMSO (i.e., 0.1 % DMSO in the droplet). As shown in Figure 3(a, b), the position of the phase boundary shifted markedly towards lower protein and lower PEG concentrations in the presence of bis-ANS, in line with previous observations on the LCD of FUS.[55] A differential map of the SVM-derived heat maps quantifies the shift of the phase boundary (Figure 3(c)), thus providing a means to quantitatively assess the effect of chemical modulators on phase behaviour.

In summary, the PhaseScan approach provides a high-resolution assessment of changes in protein LLPS behaviour upon small-molecule addition. This feature is significant, as the effect of many candidate molecules is likely to be subtle, and identification of potential hits from a naïve candidate panel would require high assay resolution. PhaseScan achieves this rapidly

with minimal sample consumption, promising efficient scale-up for high-content library screening.
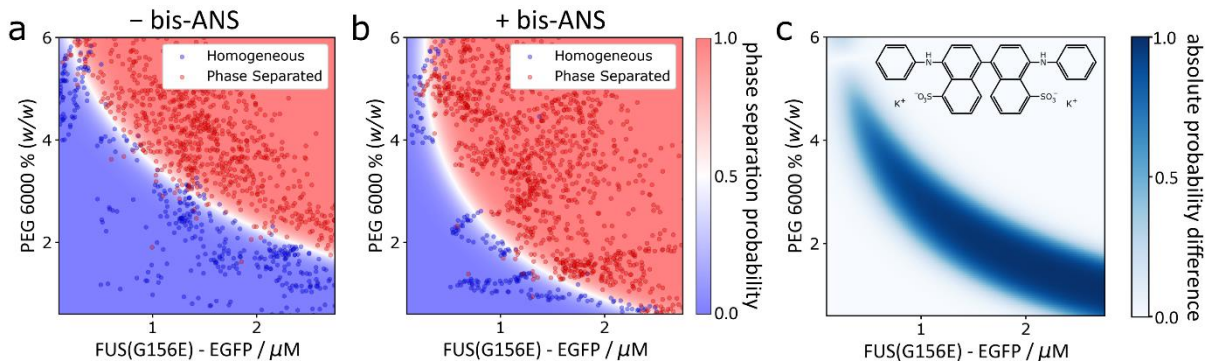

Figure 3: Probing the effect of small molecule modulators on phase separation using PhaseScan. **(a)** Control phase diagram of EGFP-tagged EGFP-tagged FUS^{G156E} vs. PEG 6000 concentration in the absence of bis-ANS. N = 1616 droplets. **(b)** Phase diagram of EGFP-tagged EGFP-tagged FUS^{G156E} vs. PEG 6000 concentration in the presence of bis-ANS. N = 2559 droplets. **(c)** Molecular structure of bis-ANS and differential phase diagram of homotypic FUS phase diagram ± bis-ANS.

Generation of multi-dimensional phase diagrams

It has been established that a variety of environmental factors can trigger or modulate LLPS, a factor that underlies their versatility in terms of the biological functions that they fulfil. Investigation of these effects is typically constrained to analysis in two-dimensional (2D) chemical space, primarily due to the impractically large number of individual experiments that must be carried out if multiple parameters are investigated simultaneously by manual methods. Since the PhaseScan platform enables automated and high-throughput generation of a wide range of solution conditions, we sought to expand the platform to enable investigation of multi-dimensional chemical space beyond conventional two dimensional phase diagrams in a single experiment, including small-molecule modulation.

To demonstrate this, we performed a three-dimensional (3D) parameter space PhaseScan experiment on FUS^{G156E}. We included 1,6-hexanediol (1,6-HD), a small molecule known to interfere with LLPS behaviour that has been employed extensively to probe LLPS systems.[19] This was added as a fourth component to the PhaseScan mix in addition to EGFP-tagged FUS^{G156E}, PEG and buffer solutions (Figure S7). Following droplet generation, trapping and imaging (~7500 droplets), the relative concentrations of each of the three barcodes was used to determine the concentrations of FUS^{G156E}, PEG and 1,6-HD present in each drop. This measurement was combined with the classification of each droplet as containing phase

separated or homogeneous protein to construct a three-dimensional phase diagram for the system (Figure 4(a, b), Supporting Movie 1). As before, the concentration of EGFP-tagged FUS^{G156E} and PEG were barcoded by the EGFP tag and the addition of Alexa647 dye, respectively, whereas the concentration of 1,6-HD was barcoded by the addition of Alexa546 (Figure 4(c)).

As observed in the 2D phase diagrams shown previously, and evident in the projection from the 3D phase diagrams (Figure 4(d–f)), phase separation was favoured at high protein and PEG concentrations. As expected, phase separation was reduced at higher concentrations of 1,6-HD, since 1,6-HD is known in disrupt protein condensation by competing for hydrophobic interactions that commonly drive protein LLPS. Notably, the antagonistic effects of molecular crowding and 1,6-HD on phase separation as a function of protein concentration are simultaneously observable (Figure 4(e–g)). We propose that the ability to assess multiple modulators of phase separation in a single experiment presents a facile, high-resolution means with which to investigate mechanistic aspects of phase separation with minimal sample consumption (<6 μL of protein solution).
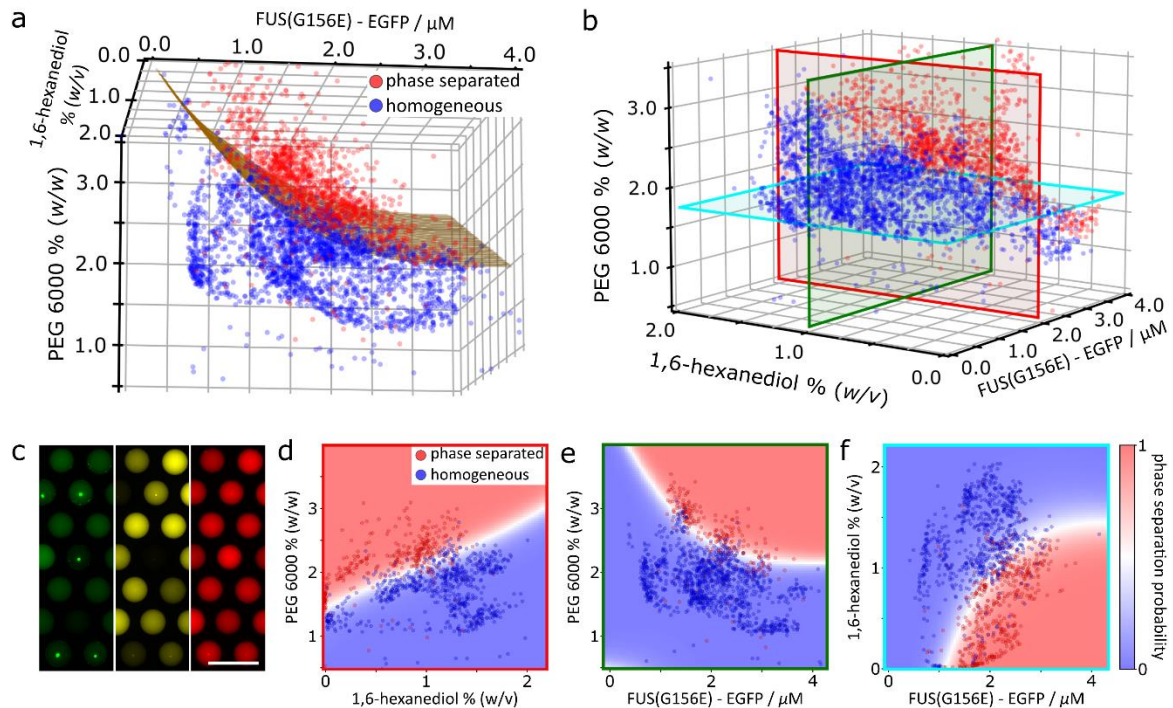

Figure 4: Generation of multidimensional phase diagrams using the PhaseScan platform. (a, b) 3D phase diagram of EGFP-tagged FUS^{G156E} vs. PEG 6000 vs. 1,6-HD concentration. N = 3904 droplets. **(c)** Epifluorescence microscopy images of trapped microdroplets with EGFP (green), Alexa546 (yellow), and Alexa647 (red) fluorescence corresponding to FUS^{G156E} and 1,6-HD, and PEG

concentrations, respectively. **(d-f)** 2D slices of the 3D phase diagram, corresponding to the red, green and blue planes shown in (b), respectively.

Conclusions

Biomolecular condensation has transformed our understanding of cell biology. Physicochemical characterisation of the parameters that control and modulate phase separation has thus become essential for an improved understanding of protein phase behaviour, including for the therapeutic modulation of LLPS phenomena. The PhaseScan platform presented herein provides a basis for the rapid and high-resolution acquisition of LLPS phase diagrams through the application of microdroplet techniques. We have demonstrated that the PhaseScan approach is applicable to a wide range of phase-separating systems ranging from coacervating peptides, human proteins and viral proteins, and provides a useful tool to enable rapid, high-resolution mechanistic analysis of phase separation processes. PhaseScan further enables the provision of high-resolution phase diagrams for the accurate quantification of the effect of small molecule modulators on the phase separation equilibrium, a feature that is essential in drug screening efforts. Uniquely, PhaseScan allows exploration of higher-dimensional chemical space in a single experiment, including the effect of small-molecule modulation, with minimal sample consumption.

We envisage that microfluidic platforms such as those presented here can find many applications in the quantitation of LLPS equilibria, such as, for example, the screening of candidate small molecules for the therapeutic modulation of phase-separation behaviour. Future work could utilise a combination of the PhaseScan and droplet-shrinking approaches,[30] whereby an initial library of droplets are produced that possess a variety of chemical conditions, before these droplets are then shrunk by evaporation. Thus, the concentration-driven onset of LLPS could be assessed in a highly parallelised manner given the large number of unique starting conditions. Indeed, we have acquired proof-of-concept of this approach by shrinking droplets containing a range of FUS156 and RNA concentrations following the conventional PhaseScan experiment (Supporting Information, Figure S8). Moreover, together with integration of microwell- automated sample handling from microwell plates, as described previously,[56] rapid screening of multiple drug-protein combinations could be achieved. We note that with the relatively low droplet generation rate we employ here (~30 Hz), future experiments could achieve an improved assay throughput by combining high-frequency droplet

14

generation with fast microscopy techniques. This approach opens a route towards high resolution and high throughput exploration of protein and nucleic acid phase behaviour.

Materials and Methods

Materials

All reagents and chemicals were purchased with the highest purity available. Tris as a buffer reagent and KCl were from Fisher Scientific. PolyU and PolyA RNA with a molecular weight range from 800–1000 kDa was purchased from Sigma Aldrich as lyophilized powder. PolyU$_{100}$ RNA was purchased from Biomers as lyophilized power and dissolved into a stock of 1 mg/mL in mQ water before use 1,6-HD was purchased from Santa Cruz Biotechnology. Bis-ANS was purchased from Invitrogen and dissolved to make a stock solution in DMSO (Sigma Aldrich). Alexa546 and Alexa647 carboxylic acid were obtained from Thermo Fisher. PEG 4000 and 6000 were from Sigma Aldrich. Details on the production of proteins (FUS^{G156E}-EGFP, G3BP1-GFP, NSP2/5, SARS-CoV-2 N and (PR)$_{25}$ are given in the Supporting Information.

Device fabrication

PDMS (Corning) devices for droplet generation and multilayer well-devices for droplet collection and imaging were produced on SU-8 (Microchem) moulds fabricated via photolithographic processes as described previously.[57–59] Further details are provided in the Supporting Information.

Droplet generation

Syringe pumps (neMESYS modules, Cetoni) were used to control flows of protein, buffer and LLPS trigger supplemented with barcoding dyes as appropriate. The aqueous flowrates were configured to vary automatically according to pre-set gradients, with constant total flow rate of 60 μL/h, to scan phase behaviour over a nominal concentration range of approximately one order of magnitude for each of the component solutions. FC-40 oil (containing 1.5% (*v*/*v*) fluorosurfactant, RAN Biotechnologies) was introduced to the device at a constant flow rate of 50−120 μL/h for generation of microdroplets of approximately 650 pL volume. Droplets were trapped in a floating droplet array[60] directly after generation. For further details see Supporting Information.

Imaging

Trapped microdroplets were imaged using an AxioObserver D1 microscope (Zeiss) equipped with a 5x air objective (Zeiss) and a high-sensitivity camera (Evolve 512, Photometrics), except

for the data in Figure 2(d) which was acquired by imaging droplets under flow, using a microscope equipped with a dichroic filter set for simultaneous multi-wavelength imaging. Appropriate filter sets were used for EFGP, Alexa Fluor 546 and Alexa Fluor 647 detection (Chroma Technology 49002, 49004 and 49006, respectively). Minimal crosstalk between fluorescence channels was observed, which was removed during the image processing and calibration procedure (see Supporting Information, Figure S9).

Droplet detection and phase diagram generation

Acquired images were analysed using a custom-written Python script. Representative data and additional details are provided in the Supporting Information (Figures S9 and S10). Briefly, droplets were fitted as circles in the images. Non-circular droplets or erroneous detections were filtered and removed. From the fitted circular areas, the total intensity was calculated and normalised to obtain the intensity per unit volume (calculated using the fitted diameter), and converted to concentrations by comparison to calibration images acquired with known barcode concentration (Figure S9). Droplets were classified as phase-separated or homogeneous according to the presence or absence of at least three connected pixels of an intensity above an algorithm-defined threshold intensity. Representative classification output is presented in the Supporting Information (Figure S10). Droplet classification and barcode concentrations were then combined on a per-droplet basis to produce phase diagrams. A Support Vector Machine algorithm was then trained on the droplet dataset to produce a probability map of phase separation over the phase-space in question.

Acknowledgements

Author Contributions

W.E.A., G.K., and T.P.J.K. conceived the study. W.E.A., N.A.E., R.Q., K.D., T.J.W., J.A., J. N.-A. and Y.X. performed experiments. R.Q. and W.E.A. developed analytical tools. T.M.F., J.G.-B., A.B., D.K., S.A., and P.St.G.-H. provided materials. W.E.A. and G.K. wrote the original draft, all authors reviewed and edited the paper.

Conflict of interest

Parts of this work have been the subject of a patent application filed by Cambridge Enterprise Limited, a fully owned subsidiary of the University of Cambridge. T.P.J.K. and P. StGH. are founders, and W.E.A. and G.K. are employees of Transition Bio Ltd.

References

1. Boeynaems, S. *et al.* Protein Phase Separation: A New Phase in Cell Biology. *Trends in Cell Biology* **28**, 420–435 (2018).

2. Hyman, A. A., Weber, C. A. & Jülicher, F. Liquid-Liquid Phase Separation in Biology. *Annual Review of Cell and Developmental Biology* **30**, 39–58 (2014).

3. Shin, Y. & Brangwynne, C. P. Liquid Phase Condensation in Cell Physiology and Disease. *Science* vol. 357 Preprint at https://doi.org/10.1126/science.aaf4382 (2017).

4. Banani, S. F., Lee, H. O., Hyman, A. A. & Rosen, M. K. Biomolecular Condensates: Organizers of Cellular Biochemistry. *Nature Reviews Molecular Cell Biology* vol. 18 285–298 Preprint at https://doi.org/10.1038/nrm.2017.7 (2017).

5. Sokolova, E. *et al.* Enhanced Transcription Rates in Membrane-Free Protocells Formed by Coacervation of Cell Lysate. *Proc Natl Acad Sci U S A* **110**, 11692–11697 (2013).

6. Kim, T. H. *et al.* Phospho-Dependent Phase Separation of FMRP and CAPRIN1 Recapitulates Regulation of Translation and Deadenylation. *Science (1979)* **365**, 825–829 (2019).

7.   Riback, J. A. *et al.* Stress-Triggered Phase Separation Is an Adaptive, Evolutionarily Tuned Response. *Cell* **168**, 1028-1040.e19 (2017).

8.   Boeynaems, S. *et al.* Phase Separation of C9orf72 Dipeptide Repeats Perturbs Stress Granule Dynamics. *Mol Cell* **65**, 1044-1055.e5 (2017).

9.   Patel, A. *et al.* A Liquid-to-Solid Phase Transition of the ALS Protein FUS Accelerated by Disease Mutation. *Cell* **162**, 1066–1077 (2015).

10.   Murakami, T. *et al.* ALS/FTD Mutation-Induced Phase Transition of FUS Liquid Droplets and Reversible Hydrogels into Irreversible Hydrogels Impairs RNP Granule Function. *Neuron* **88**, 678–690 (2015).

11.   Bouchard, J. J. *et al.* Cancer Mutations of the Tumor Suppressor SPOP Disrupt the Formation of Active, Phase-Separated Compartments. *Molecular Cell* **72**, 19-36.e8 (2018).

12.   Geiger, F. *et al.* Rotavirus Replication Factories Are Complex Ribonucleoprotein Condensates. *bioRxiv* Preprint at https://doi.org/10.1101/2020.12.18.423429 (2020).

13.   Mullard, A. Biomolecular Condensates Pique Drug Discovery Curiosity. *Nature Reviews Drug Discovery* (2019) doi:10.1038/d41573-019-00069-w.

14.   Wheeler, R. J. *et al.* Small Molecules for Modulating Protein Driven Liquid-Liquid Phase Separation in Treating Neurodegenerative Disease. *bioRxiv* 721001 (2019) doi:10.1101/721001.

15.   Li, Q. *et al.* LLPSDB: A Database of Proteins Undergoing Liquid-Liquid Phase Separation in Vitro. *Nucleic Acids Research* **48**, D320–D327 (2020).

16.   Alberti, S., Gladfelter, A. & Mittag, T. Considerations and Challenges in Studying Liquid-Liquid Phase Separation and Biomolecular Condensates. *Cell* **176**, 419–434 (2019).

17.   Riback, J. A. *et al.* Composition-Dependent Thermodynamics of Intracellular Phase Separation. *Nature* 1–6 (2020) doi:10.1038/s41586-020-2256-2.

18.   Braun, M. K. *et al.* Reentrant Phase Behavior in Protein Solutions Induced by Multivalent Salts: Strong Effect of Anions Cl - Versus NO 3-. *Journal of Physical Chemistry B* **122**, 11978–11985 (2018).

19. Kroschwald, S., Maharana, S. & Simon, A. Hexanediol: A Chemical Probe to Investigate the Material Properties of Membrane-Less Compartments. *Matters (Zur)* (2017) doi:10.19185/matters.201702000010.

20. Nott, T. J., Craggs, T. D. & Baldwin, A. J. Membraneless organelles can melt nucleic acid duplexes and act as biomolecular filters. *Nature Chemistry* **8**, 569–575 (2016).

21. Nott, T. J. *et al.* Phase Transition of a Disordered Nuage Protein Generates Environmentally Responsive Membraneless Organelles. *Molecular Cell* **57**, 936–947 (2015).

22. Farahi, N., Lazar, T., Wodak, S. J., Tompa, P. & Pancsa, R. Integration of Data from Liquid–Liquid Phase Separation Databases Highlights Concentration and Dosage Sensitivity of LLPS Drivers. *International Journal of Molecular Sciences 2021, Vol. 22, Page 3017* **22**, 3017 (2021).

23. Wheeler, R. J. Therapeutics—How to Treat Phase Separation-Associated Diseases. *Emerging Topics in Life Sciences* (2020) doi:10.1042/ETLS20190176.

24. Alberti, S. & Dormann, D. Liquid–Liquid Phase Separation in Disease. *Annual Review of Genetics* **53**, 171–194 (2019).

25. Klamser, J. U., Kapfer, S. C. & Krauth, W. Thermodynamic Phases in Two-Dimensional Active Matter. *Nature Communications* **9**, 5045 (2018).

26. Bracha, D. *et al.* Mapping Local and Global Liquid Phase Behavior in Living Cells Using Photo-Oligomerizable Seeds. *Cell* **175**, 1467-1480.e13 (2018).

27. Brangwynne, C. P., Tompa, P. & Pappu, R. V. Polymer Physics of Intracellular Phase Transitions. *Nature Physics* **11**, 899–904 (2015).

28. Yang, P. *et al.* G3BP1 Is a Tunable Switch that Triggers Phase Separation to Assemble Stress Granules. *Cell* **181**, 325-345.e28 (2020).

29. Peskett, T. R. *et al.* A Liquid to Solid Phase Transition Underlying Pathological Huntingtin Exon1 Aggregation. *Molecular Cell* **70**, 588-601.e6 (2018).

30. Kopp, M. R. G. *et al.* Microfluidic Shrinking Droplet Concentrator for Analyte Detection and Phase Separation of Protein Solutions. *Analytical Chemistry* **92**, 5803–5812 (2020).

31.   Taylor, N. *et al.* Biophysical characterization of organelle-based RNA/protein liquid phases using microfluidics. *Soft Matter* **12**, 9142–9150 (2016).

32.   Celetti, G. *et al.* The Liquid State of FG-Nucleoporins Mimics Permeability Barrier Properties of Nuclear Pore Complexes. *J Cell Biol* e201907157 (2020) doi:10.1083/jcb.201907157.

33.   Bremer, A., Mittag, T. & Heymann, M. Microfluidic characterization of macromolecular liquid–liquid phase separation. *Lab on a Chip* **20**, 4225–4234 (2020).

34.   Selimović, E., Gobeaux, F. & Fraden, S. Mapping and manipulating temperature–concentration phase diagrams using microfluidics. *Lab on a Chip* **10**, 1696–1699 (2010).

35.   Li, P. *et al.* Rapid Determination of Phase Diagrams for Biomolecular Liquid–Liquid Phase Separation with Microfluidics. *Analytical Chemistry* **94**, 687–694 (2022).

36.   Murakami, T. *et al.* ALS/FTD Mutation-Induced Phase Transition of FUS Liquid Droplets and Reversible Hydrogels into Irreversible Hydrogels Impairs RNP Granule Function. *Neuron* **88**, 678–690 (2015).

37.   Song, H., Tice, J. D. & Ismagilov, R. F. A microfluidic system for controlling reaction networks in time. *Angewandte Chemie - International Edition* (2003) doi:10.1002/anie.200390203.

38.   Agresti, J. J. *et al.* Ultrahigh-Throughput Screening in Drop-Based Microfluidics for Directed Evolution. *Proc Natl Acad Sci U S A* **107**, 4004–9 (2010).

39.   Labanieh, L., Nguyen, T. N., Zhao, W. & Kang, D. K. Floating droplet array: An ultrahigh-throughput device for droplet trapping, real-time analysis and recovery. *Micromachines (Basel)* **6**, (2015).

40.   Sagui, C., Stinson O'gorman, D. & Grant, M. Nucleation, growth and coarsening in phase-separating systems. *Scanning Microscopy* **12**, 3–8 (1998).

41.   Marqusee, J. A. & Ross, J. Kinetics of phase transitions: Theory of Ostwald ripening. *The Journal of Chemical Physics* **79**, 4710 (1983).

42.   Linsenmeier, M. *et al.* Dynamics of Synthetic Membraneless Organelles in Microfluidic Droplets. *Angewandte Chemie International Edition* **58**, 14489–14494 (2019).

43. Banerjee, P. R., Milin, A. N., Moosa, M. M., Onuchic, P. L. & Deniz, A. A. Reentrant Phase Transition Drives Dynamic Substructure Formation in Ribonucleoprotein Droplets. *Angewandte Chemie International Edition* **56**, 11354–11359 (2017).

44. Krainer, G. *et al.* Reentrant liquid condensate phase of proteins is stabilized by hydrophobic and non-ionic interactions. *Nature Communications 2021 12:1* **12**, 1–14 (2021).

45. Wang, J. *et al.* A Molecular Grammar Governing the Driving Forces for Phase Separation of Prion-like RNA Binding Proteins. *Cell* **174**, 688-699.e16 (2018).

46. Guillén-Boixet, J. *et al.* RNA-Induced Conformational Switching and Clustering of G3BP Drive Stress Granule Assembly by Condensation. *Cell* **181**, 346-361.e17 (2020).

47. Portz, B. & Shorter, J. Biochemical Timekeeping Via Reentrant Phase Transitions. *Journal of Molecular Biology* **433**, 166794 (2021).

48. Nikolic, J. *et al.* Negri bodies are viral factories with properties of liquid organelles. *Nature Communications* **8**, 1–12 (2017).

49. Guseva, S. *et al.* Measles virus nucleo- And phosphoproteins form liquid-like phase-separated compartments that promote nucleocapsid assembly. *Science Advances* **6**, eaaz7095 (2020).

50. Geiger, F. *et al.* Liquid–liquid phase separation underpins the formation of replication factories in rotaviruses. *The EMBO Journal* e107711 (2021) doi:10.15252/EMBJ.2021107711.

51. Perdikari, T. M. *et al.* SARS-CoV-2 nucleocapsid protein phase-separates with RNA and with human hnRNPs. *The EMBO Journal* **39**, (2020).

52. Lu, S. *et al.* The SARS-CoV-2 nucleocapsid phosphoprotein forms mutually exclusive condensates with RNA and the membrane-associated M protein. *Nature Communications* **12**, (2021).

53. Dolgin, E. Drug startups coalesce around condensates. *Nature Biotechnology* **39**, 123–125 (2021).

54. Klein, I. A. *et al.* Partitioning of cancer therapeutics in nuclear condensates. *Science (1979)* **368**, 1386–1392 (2020).

55.   Babinchak, W. M. *et al.* Small molecules as potent biphasic modulators of protein liquid-liquid phase separation. *Nature Communications* **11**, (2020).

56.   Longwell, S. A. & Fordyce, P. M. MicrIO: An open-source autosampler and fraction collector for automated microfluidic input-output. *Lab on a Chip* **20**, 93–106 (2020).

57.   McDonald, J. C. *et al.* Fabrication of Microfluidic Systems in Poly(dimethylsiloxane). *Electrophoresis* **21**, 27–40 (2000).

58.   Arter, W. E. *et al.* Digital Sensing and Molecular Computation by an Enzyme-Free DNA Circuit. *ACS Nano* (2020) doi:10.1021/acsnano.0c00628.

59.   Mazutis, L. *et al.* Single-Cell Analysis and Sorting Using Droplet-Based Microfluidics. *Nat. Protocols* **8**, 870–891 (2013).

60.   Labanieh, L., Nguyen, T. N., Zhao, W. & Kang, D. K. Floating droplet array: An ultrahigh-throughput device for droplet trapping, real-time analysis and recovery. *Micromachines (Basel)* **6**, (2015).